Advances in Full-Wave Modeling of Radio Frequency Heated, Multi-dimensional Plasmas

E. F. Jaeger, L. A. Berry, E. D'Azevedo, D. B. Batchelor, M. D. Carter, and K. F. White

P.O. Box 2009, Oak Ridge National Laboratory, Oak Ridge, Tennessee 37831-8071

H. Weitzner

Courant Institute of Mathematical Sciences, New York University, New York, New York 10012

Previous full-wave models for radio frequency (rf) heating in multi-dimensional plasmas have relied on either cold-plasma or finite Larmor radius approximations. These models assume that the perpendicular wavelength of the rf field is much larger than the ion Larmor radius, and they are therefore limited to relatively long wavelengths and low cyclotron harmonics. Recently, alternate full-wave models have been developed that eliminate these restrictions. These "all orders spectral algorithms" (AORSA) take advantage of new computational techniques for massively parallel computers to solve the integral form of the wave equation in multiple dimensions without any restriction on wavelength relative to orbit size, and with no limit on the number of cyclotron harmonics retained. These new models give high-resolution, two-dimensional solutions for mode conversion and high harmonic fast wave heating in tokamak geometry. In addition, they have been extended to give fully three-dimensional solutions of the integral wave equation for minority ion cyclotron heating in stellarator geometry. By combining multiple periodic solutions for individual helical field periods, it is possible to obtain complete wave solutions valid over the entire volume of the stellarator for arbitrary antenna geometry.

I. INTRODUCTION

Numerical calculations of wave propagation and heating in multi-dimensional plasmas have generally been of two types: geometrical optics (or ray tracing), and full-wave or global calculations. Full-wave models are needed because ray tracing does not optimally treat realistic antenna spectra, plasma cutoffs, or mode conversion layers, nor does it include large-scale coherent effects such as diffraction, interference, and wave focussing. Early two-dimensional (2-D) full-wave models [1–4] were based on finite difference and finite element algorithms in both the radial and poloidal directions. In addition, finite Larmor radius (FLR) expansions ($k_\perp \rho << 1$, where $k_\perp$ is the perpendicular wave number and ρ is the ion Larmor radius) were used to express the plasma current as a differential operator. The parallel gradient operator ($ik_\parallel = \hat{e}_b \cdot \nabla$), however, couples to the poloidal direction, and is not easily treated with finite differences because it appears in the argument of the plasma dispersion function, effectively raising the order of the wave equation to infinity. Therefore, these early models neglected the spatial variation of the parallel wave vector ($k_\parallel$), and as a result, underestimated electron Landau damping (ELD).[5]

More recent full-wave models such as PICES [5] and TORIC [6] have used a superposition of Fourier modes in the poloidal direction to represent the wave field, thus reducing the parallel gradient to an algebraic operator. These codes accurately calculate the electron damping rate, but still rely on FLR expansions in the radial direction to express the plasma current as a differential operator. In practice, they are limited to relatively long wavelengths and cyclotron harmonics of two or less (because each cyclotron harmonic raises the radial order of the differential equation by two). In addition, the magnetic flux coordinates required for the poloidal mode expansion are singular at the origin, and often lead to numerical problems near the magnetic axis.

Recently, alternate full-wave models [7–9] have been developed that eliminate these difficulties. These all-orders, spectral algorithms (AORSA) [8, 9] solve the integral form of the wave equation with no assumption regarding the smallness of $k_\perp \rho$ and no limit on the number of cyclotron harmonics retained. The earliest example of such a model is the one-dimensional (1-D)

METS95 code [7] developed by D. N. Smithe. Ion Bernstein waves (IBWs) are formed naturally in these models and are correctly absorbed by Landau damping, even when $k_\perp\rho$ exceeds unity. Furthermore, the use of cylindrical coordinates rather than flux coordinates moves the singular axis outside of the plasma volume and hence eliminates all numerical problems associated with the magnetic axis. However, because all modes in the spectral representation are coupled, these new models require the calculation and inversion of very large, dense matrices. In contrast, FLR codes such as PICES and TORIC require only the inversion of matrices that, while of comparable size, are sparse and banded. For this reason, spectral calculations to all orders in $k_\perp\rho$ have so far been limited to only one spatial dimension.[7, 8]

In this paper, we extend these methods to multiple dimensions by taking advantage of new matrix inversion algorithms for distributed-memory parallel computers.[10] Numerical convergence is improved by writing the equations in the laboratory frame of reference rather than in local magnetic coordinates. One disadvantage of the laboratory frame is that it is more difficult to express the plasma conductivity which must be corrected to first order in ρ/L (where L is the equilibrium scale length) to take into account the spatial variation of the transformation from laboratory to local magnetic coordinates. This preserves cancellations between electron Landau damping and magnetic pumping, and ensures accuracy in calculating the relative fractions of power absorbed by ions and electrons.

The remainder of this article is organized as follows. Section II describes the AORSA algorithm in three dimensional (3-D) toroidal geometry. Section III transforms the plasma conductivity tensor from local magnetic coordinates to the laboratory frame of reference. Section IV discusses the numerical method, and Sects. V through VII describe applications to mode conversion and heating in tokamak and stellarator plasmas. Results are summarized in Sect. VIII.

II. THE "ALL-ORDERS SPECTRAL ALGORITHM" (AORSA)

For time harmonic wave fields with frequency ω, Ampere's and Faraday's laws combine

to give the inhomogeneous wave equation, or *Helmholtz equation*

$$-\nabla\times\nabla\times\mathbf{E}+\frac{\omega^2}{c^2}\left(\mathbf{E}+\frac{i}{\omega\epsilon_0}\mathbf{J}_p\right)=-i\omega\mu_0\mathbf{J}_{ant} \tag{1}$$

where **E** is the wave electric field, and $\mathbf{J}_{ant}$ is a specified external antenna current. Most of the complication in Eq. (1) arises from the response of the plasma to the electromagnetic wave field, which is included through the plasma current, $\mathbf{J}_p$. For a non-uniform medium, the relationship between the plasma current and the wave electric field is a non-local operator, and can be expressed to lowest order in ρ/L as an integral of the form [11]

$$\mathbf{J}_p(\mathbf{r})=\int d\mathbf{r}'\ \sigma(\mathbf{r}\,,\ \mathbf{r}'-\mathbf{r}\,)\cdot\mathbf{E}\,(\mathbf{r}'\,) \tag{2}$$

where **r** is the position vector, and $\sigma(\mathbf{r}, \mathbf{r}-\mathbf{r}')$ is the *plasma conductivity kernel*.

We apply the "all-orders spectral algorithm" (AORSA) [7–9] to solve Eqs. (1) and (2) in multi-dimensional geometries. With this method, we retain all orders in $k_\perp\rho$, while at the same time assuming a locally homogeneous plasma [8] ($\rho/L \ll 1$). The geometry is conveniently described by cylindrical coordinates (R, φ, Z) where R is the radial position measured from the toroidal axis, φ is the toroidal angle, and Z is the vertical position. The radio frequency (rf) electric field is expanded in Fourier harmonics as

$$\mathbf{E}(x,y,\varphi)=\sum_{n,\,m,\,l}\mathbf{E}_{n,m,l}\ e^{i(k_n x+k_m y+l\varphi)} \tag{3}$$

where $x = R - R_0$, $y = Z$, and n, m, and l are Fourier mode numbers. In the limit of a spatially homogeneous plasma, σ depends only on $\mathbf{r}-\mathbf{r}'$, and the convolution theorem can be used to recast Eq. (2) in Fourier space [11]

$$\mathbf{J}_p(x,y,\varphi)=\sum_{n,\,m,\,l}\underline{\underline{\sigma}}(k_n,k_m,l)\cdot\mathbf{E}_{n,\,m,\,l}\ e^{i(k_n x+k_m y+l\varphi)} \tag{4}$$

where $\sigma(k_n, k_m, l)$ is the Fourier coefficient of the conductivity kernel, or the *plasma conductivity tensor*. To provide a lowest order description in ρ/L of an inhomogeneous plasma, we include additional spatial dependence in σ from variation in plasma parameters such as density, temperature, and magnetic field. For tokamak geometry with symmetry about the toroidal axis, the φ harmonics are uncoupled and each can be calculated separately. For stellarator geometry with toroidal inhomogeneity, the φ harmonics are coupled and must be calculated simultaneously.

III. PLASMA CONDUCTIVITY IN THE LABORATORY FRAME

Equation (1) can be solved in either local magnetic coordinates [12] (the "Stix" frame), or in laboratory coordinates. Previous full-wave rf models [5, 6] have used the Stix frame because $E_\parallel$ (which is $<< E_\perp$) is calculated directly as one of the unknowns in the system. In AORSA, we work instead in the laboratory frame because it exhibits better convergence properties in Fourier space and because the Fourier components $(\nabla \times \nabla \times \mathbf{E})_{n,m,l}$ are explicitly divergence free.[13] One disadvantage of the laboratory frame is that $E_\parallel$ is not determined directly in the solution, but instead comes indirectly from a linear combination of the larger electric field components E_R, E_φ, and E_Z. Because $E_\parallel$ is much smaller than $E_\perp$, a highly accurate solution is required to resolve $E_\parallel$.

Stix [12] has derived the plasma conductivity in local magnetic coordinates assuming a spatially uniform Maxwellian plasma with straight magnetic field lines and wave propagation perpendicular to both the magnetic field and the flux surface. Both Stix and Swanson [14] have adapted this result to a more general orientation of $\mathbf{k}_\perp$. To derive the plasma conductivity in the laboratory frame, the rf electric field in the orbit integral must be transformed (rotated) from the laboratory frame to Stix coordinates, $\mathbf{E}_k^{Stix}(\mathbf{r}) \exp(i\mathbf{k}_{Stix}\cdot\mathbf{r}) = \mathbf{U}(\mathbf{r}) \cdot \mathbf{E}_k^{Lab} \exp(i\mathbf{k}_{Lab}\cdot\mathbf{r})$, where $\mathbf{U}$ is a matrix depending on the direction of the magnetic field and $\mathbf{k}_{Stix} = \mathbf{U} \cdot \mathbf{k}_{Lab}$. The spatial dependence of $\mathbf{U}$ on $\mathbf{r}$ results in an additional complication in evaluating the characteristic integral that is central to the derivation of the conductivity tensor. Because the spatial dependence of $\mathbf{U}$ is much weaker than that of the exponential, we approximate $\mathbf{U}$ with a Taylor series expansion,

$$\mathbf{U}(\mathbf{r}') \approx \mathbf{U}(\mathbf{r}) + \nabla_\perp \mathbf{U} \cdot (\mathbf{r}' - \mathbf{r}) \ , \tag{5}$$

where $\mathbf{r}'$ is the position of a particle at time t', and the gradient is taken in the Stix frame. This expansion assumes that corrections to the spectrum caused by excursions of the orbit away from the guiding center as a result of the rotation $\mathbf{U}$ are of order ρ/L . The parallel component of $\nabla\mathbf{U}$ represents additional dispersion in $k_\parallel$ along the characteristic integral, and cannot be treated as a perturbation because of the singular plasma response at the Doppler resonance. For simplicity, it is omitted here.

Using the Taylor series expansion in Eq. (5), the orbit integral can be evaluated to obtain the final expression for the plasma conductivity in the laboratory frame,

$$\sigma_{lab} = \mathbf{U}^{-1} \cdot \sigma_{Stix} \cdot \mathbf{U} \ - \ i \left(\mathbf{U}^{-1} \cdot \frac{\partial \sigma_{Stix}}{\partial \mathbf{k}} \cdot \nabla_\perp \mathbf{U} \right) \tag{6}$$

where σ_{Stix} is the generalization of the Stix conductivity as given by Swanson.[14] The first term in Eq. (6) represents a simple rotation from local coordinates to the laboratory frame, and the second term is a first-order correction in ρ/L arising from the spatial dependence of the rotation matrix in the orbit integral. This term is needed to preserve the cancellation [15] between transit-time magnetic pumping and Landau damping, and to ensure accuracy in calculating the relative fractions of power absorbed by ions and electrons.[9]

IV. NUMERICAL METHOD

The *method of collocation* [16] is used to write Eq. (1) at each point on a spatial mesh, and the resulting set of linear equations is solved for the Fourier coefficients, $\mathbf{E}_{n,m,l}$. This avoids convolutions associated with the plasma current, and at the same time, includes cyclotron harmonics of arbitrary order. Furthermore, boundary conditions are easily implemented at specified positions in space. However, because all modes in the spectral representation are coupled, the complete

solution requires calculating and inverting a very large, dense matrix. For example, with 200×200 Fourier modes in 2-D, or equivalently, $50 \times 50 \times 16$ modes in 3-D, it is necessary to solve 120,000 coupled complex equations, and the storage required for the resulting matrix is ~ 230 Gbytes. Such large amounts of memory are seldom available on a single processor. However, with the availability of large parallel computers, it is possible to distribute the required memory over many processors, and the distributed matrix can be inverted using ScaLAPACK,[10] a library of high-performance linear algebra routines for distributed-memory, parallel computers. Problem size scales as the square root of the number of processors as shown in Fig. 1(a). Using 576 processors on the Oak Ridge National Laboratory IBM RS/6000 SP computer, up to 120,000 coupled complex equations can be solved, while achieving 0.66 teraflops (660 billion operations per second) during matrix factorization. With a still larger computer, such as the NERSC-II super computer with 2000 processors, at least twice this number of equations can be solved. Computing speed scales linearly with the number of processors, as shown in Fig. 1(b), and there is no indication of saturation caused by communication between processors.

V. MODE-CONVERSION IN TWO DIMENSIONS

With these techniques, it is possible to obtain fully converged 2-D solutions that resolve the short-wavelength ion Bernstein waves (IBW) excited near the two-ion-hybrid resonance layer in toroidal geometry. Previous attempts to model mode conversion in 2-D have had physics uncertainties because of the FLR expansion ($k_\perp \rho << 1$). However, by choosing a spectral representation with 400 modes in the horizontal dimension and 100 modes in the vertical dimension, we have obtained convergence for cases in which the mode-converted IBW is moderately absorbed.

Figure 2 shows an all-orders spectral calculation for mode-conversion in 2-D, neglecting the poloidal magnetic field. Fast wave power is launched into a deuterium plasma with a 25% helium-3 minority. Parameters are modeled after the Alcator C-Mod experiment.[17] To simplify the calculation and make convergence easier, the central temperatures are chosen large enough (10

keV) that the IBW is moderately absorbed, but small enough that the waves propagate for several wavelengths away from the resonance. Contours of the wave electric field are plotted in Fig. 2(a). The dashed curves show the mode conversion surfaces calculated from a 1-D cold plasma model. The surface associated with the majority deuterium resonance appears on the extreme left side of the plasma, and the surface associated with the minority helium-3 resonance intersects the equatorial plane near the plasma center. Figure 2(b) shows a blowup of the helium-3 resonance region (dashed box) where the individual wave fronts of the IBW are clearly visible. Because IBW is a "backward" wave, the wave fronts in Fig. 2(b) propagate to the right in time, or opposite to the direction of the group velocity and energy flow. For large values of k_x and k_y, rapidly decreasing mode amplitudes indicate that this result is fully converged. As the wave energy propagates away from the resonance region, the IBW is correctly absorbed by electron Landau damping even for the dominant wavelengths in Fig. 2 that have $k_\perp\rho \sim 1.6$.

Figure 3 shows a similar calculation that includes the effect of the poloidal magnetic field, B_ϑ. Fast-wave power is launched into a deuterium plasma with a 33% hydrogen minority. Parameters are modeled after DIII-D.[18, 19] The effect of the poloidal field is to introduce a strong up-down asymmetry in the mode-converted IBW. This is partly due to the natural up-down asymmetry of the antenna's radiated power spectrum [20] and partly due to variation in the $k_\parallel$ spectrum caused by B_ϑ. When the direction of either B_ϑ or the antenna phasing is reversed, the asymmetry is also reversed, and the mode-converted IBW becomes more predominant below the midplane.

VI. HIGH-HARMONIC FAST-WAVE HEATING IN TWO DIMENSIONS

The primary heating system in the National Spherical Torus Experiment (NSTX) [21] is designed to operate at high harmonics of the ion cyclotron frequency. A self-consistent treatment of this scenario requires a large number of ion cyclotron harmonics as well as all orders in $k_\perp\rho$. Figure 4 shows a 2-D spectral calculation for NSTX shot #105830 including 20 cyclotron har-

monics and 140 Fourier modes in the *x* and *y* directions. Fast waves are launched from the low field side of a deuterium plasma with a 3.7% hydrogen minority. A Solov'ev [22] equilibrium is assumed with parameters modeled after the NSTX geometry.[23] In Fig. 4, nearly 100% of the rf power is absorbed in the first pass by Landau damping on the electrons [Fig. 4(b)]. The remaining small fraction of power is absorbed by the minority ion component at the 4*th* and 5*th* harmonics of hydrogen. These high harmonic layers are visible in the ion heating contours in Fig. 4(c). In Fig. 5, a flux surface average of the electron absorption contours in Fig. 4(b) shows that the electron heating is peaked near the magnetic axis for this case. Antenna loading (proportional to plasma absorption) is highest when the antenna is phased to drive current in the same direction as the plasma current.[20]

VII. MINORITY ION HEATING IN 3-D STELLARATOR GEOMETRY

Recent ICRF heating experiments on the Large Helical Device (LHD)[24] have demonstrated that direct ion heating by fast waves is a dominant heating mechanism for the antenna configuration and frequency used in LHD. Figure 6 shows the 3-D magnetic field geometry for LHD calculated from the VMEC code [25] with fixed boundaries. Flux surfaces and magnetic field strength are shown at four equally spaced toroidal angles within a single helical field period. The heavy dashed lines show the location of the fundamental ion cyclotron resonance for hydrogen. Figure 7 shows a 3-D rf solution for this geometry assuming identical antennas in each helical field period and using 50 modes in both the *x* and *y* directions and 16 coupled modes in the toroidal direction. A helium plasma is assumed with a 5% hydrogen minority. The antenna is centered in the $\varphi = 0$ plane, and assumed to have monopole phasing with frequency $f = 44$ MHz. Figure 7(a) shows contours of the wave electric field, and Fig. 7(b) shows contours of the minority ion heating at the four toroidal angles within the field period. The ion heating is peaked at the two-ion-hybrid resonance which is close to the ion cyclotron resonance for hydrogen in this case.

The strong parallel magnetic field gradients in this 3-D geometry cause significant broad-

ening of the plasma dispersion function near $k_{\|} = 0$. In order to obtain the converged solution in Fig. 7, it is necessary to include this broadening by using an approximate form for the generalized plasma dispersion function as suggested by Brambilla.[26]

Because the solution in Fig. 7 assumes identical antennas in each field period, periodic boundary conditions can be applied in the toroidal direction, and the Fourier basis set in φ can be reduced to exp($l\, N_p\varphi$), where N_p is the number of helical field periods. Thus, for $N_p = 10$, the basis set includes only the elements: 1, $e^{\pm 10\,\varphi}$, $e^{\pm 20\,\varphi}$, ... etc. For arbitrary antenna geometry, the full basis set exp($l\,\varphi$) is required, and the number of equations is increased by a factor of 10 for the above example. A problem of this size is beyond the capability of even our largest computers. However, by taking advantage of the underlying plasma symmetry, it is possible to obtain the complete 3-D solution for arbitrary antenna geometry by combining a number of smaller periodic solutions as in Fig. 7. To see this, consider the general form of the linear wave equation

$$L(R, \varphi\,,\, Z)\ \mathbf{E}(R, \varphi\,,\, Z) = \mathbf{F}(R, \varphi\,,\, Z) \tag{7}$$

where $L(R, \varphi\,, Z)$ represents the linear operator on the left side of Eq. (1), and $\mathbf{F}(R, \varphi\,, Z)$ represents the driving term due to the antenna current. We assume that $L(R, \varphi, Z)$ has a periodicity of $2\pi / N_p$ so that $L(R, \varphi + 2\pi/ N_p\,, Z) = L(R, \varphi\,, Z)$. We also assume that the source term $\mathbf{F}$ is non-zero only in the first field period where $0 < \varphi < 2\pi/ N_p$ (i.e., a single antenna in one field period only). To solve Eq. (7) subject to the periodicity condition for the full torus, $\mathbf{E}(R, \varphi + 2\pi, Z) = \mathbf{E}(R, \varphi, Z)$, we first construct solutions for the individual field periods from the complete set of modes,

$$\mathbf{E}_M(R, \varphi,\ Z) = \sum_{n,\ m,\ l} \mathbf{E}^M_{n,m,l}\ \ e^{i[k_n x + k_m y + (lN_p + M)\varphi]} \tag{8}$$

where M denotes the field period number ($0 \le M \le N_p - 1$). Note that for $M = 0$, Eq. (8) corresponds to the periodic solution in Fig. 7 with the boundary condition:

$$\mathbf{E_0}\left(R,\ \frac{2\pi}{N_p},\ Z\right) = \mathbf{E_0}(R,\ 0,\ Z) \quad . \tag{9}$$

For $M \neq 0$, a more general boundary condition is implied:

$$\mathbf{E}_M\left(R,\ \frac{2\pi}{N_p},\ Z\right) = \mathbf{E}_M(R\,, 0,\ Z)\ \ e^{i\,\frac{2\pi}{N_p}M} \quad . \tag{10}$$

The complete solution on the interval $0 < \varphi < 2\pi$, with the antenna in the first cavity only, can be constructed from Eq. (8) as follows. For the interval $2\pi/\ N_p\ (p-1) < \varphi < (2\pi/\ N_p)\ p$, we write the full solution as

$$\mathbf{E}(R, \varphi,\ Z) = \frac{1}{N_p}\sum_{M=0}^{N_p-1}\ \ e^{2\pi i\frac{M}{N_p}(p-1)}\ \mathbf{E}_M\left(R,\ \varphi - \frac{2\pi}{N_p}[p-1],\ Z\right) \tag{11}$$

where $p = M + 1$. To see that this satisfies the complete problem, substitute Eq. (11) into Eq. (7). The left side of Eq. (7) gives

$$L(R, \varphi,\ Z)\ \mathbf{E}(R, \varphi,\ Z) = \frac{F\left(R,\ \varphi - \frac{2\pi}{N_p}(p-1),\ Z\right)}{N_p}\sum_{M=0}^{N_p-1}\ \ e^{2\pi i\frac{M}{N_p}(p-1)} \quad . \tag{12}$$

The sum over M in Eq. (12) equals zero except for $p = 1,\ N_p+1,\ 2N_p+1, \ldots$ where it equals N_p. Thus,

$$L(R, \varphi,\ Z)\ \mathbf{E}(R, \varphi,\ Z) = \begin{cases} F(R,\ \varphi,\ Z)\ \text{ for }\ p\ =\ 1,\ N_p+1,\ 2N_p+1,\ \ldots \\ 0 \qquad\qquad\qquad\qquad\qquad\qquad \text{otherwise,} \end{cases} \tag{13}$$

and $\mathbf{E}(R, \varphi, Z)$ satisfies the wave equation with the source term (antenna) in the first cavity only ($p = 1,\ N_p+1,\ 2N_p+1, \ldots$). Furthermore, $\mathbf{E}$ is periodic on the interval 2π because each $\mathbf{E}_M$ in the sum in Eq. (11) is periodic on 2π.

Figure 8 shows the complete 3-D solution for LHD with 10 helical field periods. The

magenta surface represents the last closed flux surface, and the individual cross sections show contours of the logarithm of the minority ion power absorption at various toroidal angles, φ. The antenna is located in the field period on the extreme right side of the figure. Notice that the heating is strongest for the planes closest to the antenna, and gets progressively weaker as the planes approach the the far left side of the figure where the distance from the antenna is maximum. The ion heating follows the two-ion-hybrid resonance layer and rotates with the helicity of the magnetic field.

VIII. DISCUSSION

All-orders spectral methods allow the solution of the integral wave equation without any restriction on wavelength relative to orbit size, and with no limit on the number of cyclotron harmonics retained. With these methods, it is possible to model very short-wavelength structures such as ion Bernstein waves, as well as wave-particle interactions at high harmonics of the ion cyclotron frequency. However, because they require large amounts of computer memory, these methods have previously been applied in 1-D only. In this paper, these calculations are extended to 2-D and 3-D by taking advantage of the massively parallel architecture of today's super computers. With this approach, the limit on attainable resolution comes, not from the theory itself, but from the size and speed of the available computer.

Numerical convergence is found to be best in the laboratory frame where the Fourier components $(\nabla \times \nabla \times \mathbf{E})_{n,m,l}$ are explicitly divergence free. In this frame, the plasma conductivity must be corrected to lowest order in ρ/L to provide sufficient accuracy in calculating the wave polarization. This correction is necessary to preserve the cancellation between transit-time magnetic pumping and Landau damping and therefore to correctly calculate the fraction of power absorbed by ions and electrons.

The new calculations have produced high-definition solutions for mode conversion in 2-D toroidal geometry. In multiple dimensions, mode conversion is found to be more complicated than

simple 1-D models suggest. In particular, the poloidal magnetic field introduces a strong up-down asymmetry in the formation of the IBW. This is partly due to the natural up-down asymmetry of the antenna's radiated power spectrum and partly due to variations in the $k_\parallel$ spectrum caused by the poloidal magnetic field.

The new calculations also allow self-consistent modeling of high-harmonic fast-wave heating in low-aspect-ratio tokamaks. Ion heating at high harmonics can now be calculated self-consistently with the wave propagation in 2-D. A flux surface average of heating contours for NSTX shot #105830 shows that electron heating is peaked near the magnetic axis.

Finally, the AORSA technique has been extended to give fully 3-D solutions for minority ion heating in stellarator geometry. Using an equilibrium magnetic field calculated from the VMEC code,[25] a $50 \times 50 \times 160$ mode solution in x, y, and φ has been obtained for excitation by a single antenna located in one helical field period. This problem is too large to be solved by direct solution. Instead, the underlying symmetry of the 10 field period system has been used to construct the 160 mode solution from 10 individual solutions of the 16 mode problem.

This work should be considered as an initial step toward multi-dimensional modeling of wave processes in the $k_\perp\rho > 1$ regime. The numerical methods described are still limited by the availability of a sufficient number of processors and by the memory on each processor. It is possible that an alternative formulation of the integral wave equation in real space, rather than in Fourier space, might yield a more diagonal matrix structure [27] and reduced storage requirements.[28] It is also possible that iterative techniques in Fourier space could offer a viable alternative to the direct solution method, thereby reducing memory requirements and allowing the solution of still larger problems. As problem size increases, and hence also the number of unknowns (N), the cost for direct methods increases as $O(N^3)$, making iterative methods with effective preconditioners very attractive because each iteration requires only $O(N^2)$ work. Direct extension to three dimensions appears to be feasible for long wavelength applications such as minority ion cyclotron heating. However, resolution of short wavelength ion Bernstein waves in 3-D will require some

numerical improvements for even moderate resolution.

ACKNOWLEDGMENTS

The authors wish to thank D. N. Smithe, C. K. Phillips, A. Jaun, O. Sauter, J. Vaclavik and M. Brambilla for helpful discussions. Research was sponsored by Oak Ridge National Laboratory, managed by UT-Battelle, LLC, for the U.S. Dept. of Energy under contract DE-AC05-00OR22725.

[1] K. Itoh, and S.- I. Itoh, A. Fukuyama, Nucl. Fusion **24**, 13 (1984) .

[2] E. F. Jaeger, D. B. Batchelor, H. Weitzner and J. H. Whealton, Comput. Phys. Commun. **40**, 33 (1986) .

[3] A. Fukuyama, K. Itoh, and S. I. Itoh, Comput. Phys. Rep. **4**, 137 (1986) .

[4] L. Villard, K. Appert, R. Gruber, and J. Vaclavik, Comput. Phys. Rep. **4**, 98 (1986) .

[5] E. F. Jaeger, D. B. Batchelor and D. C. Stallings, Nucl. Fusion **33**, 179 (1993).

[6] M. Brambilla and T. Krucken, Nucl. Fusion **28**, 1813 (1988).

[7] D. N. Smithe, C. K. Phillips, J. C. Hosea, *et al*., "Investigation of RF Absorption by Fast Ions and High Temperature Plasmas using the "METS95" Wave Analysis Tool," in *Proceedings of the 12th Topical Conference on Radio Frequency Power in Plasmas*, 1997 Savannah, GA, Edited by P. M. Ryan and T. Intrator (American Institute of Physics, New York, 1997), p. 367–370.

[8] E. F. Jaeger, L. A. Berry, and D. B. Batchelor, Phys. Plasmas **7**, 3319 (2000).

[9] E. F. Jaeger, L. A. Berry, E. D'Azevedo, D. B. Batchelor, and M. D. Carter, Phys. Plasmas **8**, 1573 (2001).

[10] J. J. Dongarra, I. S. Duff, D. C. Sorensen, and H. A. van der Vorst, *Numerical Linear Algebra for High-Performance Computers* (SIAM, Philadelphia, PA, 1998).

[11] M. Brambilla, *Kinetic Theory of Plasma Waves*, (Clarendon Press, Oxford, 1998), pp. 18–20.

[12] T. H. Stix, *Waves in Plasmas* (American Institute of Physics, New York, 1992), pp. 250–256.

[13] Vdovin, V., Watari, T., Fukuyama, A., "3-D Maxwell-Vlasov Boundary Value Problem Solution in Stellarator Geometry in Ion-Cyclotron Frequency Range," in *Proceedings of the 1996 Int. Conf. on Plasma Phys.*, Nagoya (1997) 1070.

[14] D. G. Swanson, Phys. Fluids **10** (1967) 428; also D. G. Swanson, *Plasma Waves*, Academic Press, New York (1989).

[15] T. H. Stix, Nucl. Fusion **15**, 737 (1975).

[16] W. G. Strang and G. J. Fix, *An Analysis of the Finite Element Method*, (Prentice-Hall, Englewood Cliffs, N.J., 1973) pp. 117–118.

[17] P. T. Bonoli, M. Brambilla, E. Nelson-Melby, *et al*., Phys. Plasmas **7**, 1886 (2000); also P. T. Bonoli, P. O'Shea, M. Brambilla, *et al*., Phys. Plasmas **4**, 1774 (1997).

[18] L.L. Lao, J. R. Ferron, R. J. Groebner, *et al*., Nucl. Fusion **30**, 1305 (1990).

[19] A. Jaun, T. Hellsten, and S. C. Chiu, Nucl. Fusion **38**, 153 (1998).

[20] E. F. Jaeger, M. D. Carter, L. A. Berry, and D. B. Batchelor, Nucl. Fusion **38**, 1 (1998).

[21] S. M. Kaye, M. Ono, Y.-K. M. Peng, *et al.*, Fusion Technology **36**, 16 (1999).

[22] L. S. Solov'ev, Sov. Phys. –JEPT **26**, 400 (1968).

[23] C. K. Phillips, private communication (October, 2001).

[24] T. Mutoh, R. Kumazawa, T. Seki, *et al*., Phys. Rev. Lett. **85**, 4530 (2000).

[25] S. P. Hirshman and J. C. Whitson, Phys. Fluids **26**, 3553 (1983).

[26] M. Brambilla, Phys. Lett. A, **188**, 376 (1994).

[27] O. Sauter and J. Vaclavik, Comput. Phys. Commun. **84**, 226 (1994).

[28] J. Vaclavik and O. Sauter, Varenna, Italy, private communication (August, 2000).

FIGURE CAPTIONS

FIG. 1. Numerical solution using ScaLAPACK:[10] (a) problem size versus the number of processors, assuming 400 MB per processor; (b) number of operations per second achieved during matrix factorization.

FIG. 2. All-orders spectral solution for mode conversion in Alcator C-Mod [17] neglecting the poloidal magnetic field. The dashed curves show the mode-conversion layers from a 1-D cold plasma model.

FIG. 3. All-orders spectral solution for mode conversion in DIII-D[18, 19] including the poloidal magnetic field. The dashed curve shows the mode-conversion layer from 1-D cold plasma theory.

FIG. 4. All-orders spectral solution for high-harmonic fast-wave heating in NSTX shot # 105830 showing contours of (a) the rf electric field, (b) the electron power absorption, and (c) the minority ion power absorption.

FIG. 5. Flux surface average of the electron heating contours in Fig. 4(b) where ρ is the flux surface label.

FIG. 6. Magnetic field geometry from VMEC [25] for four equally spaced toroidal angles in a single helical field period of LHD [24]

FIG. 7. All orders spectral calculation of minority ion cyclotron heating for a single helical field period of LHD [24]: (a) contours of the wave electric field, and (b) contours of minority ion heating.

FIG. 8. All orders spectral calculation of minority ion cyclotron heating for all 10 field periods of LHD[24] with a single antenna located at the extreme right side of the figure. Individual cross sections show the logarithm of the minority ion power absorption at various toroidal angles.

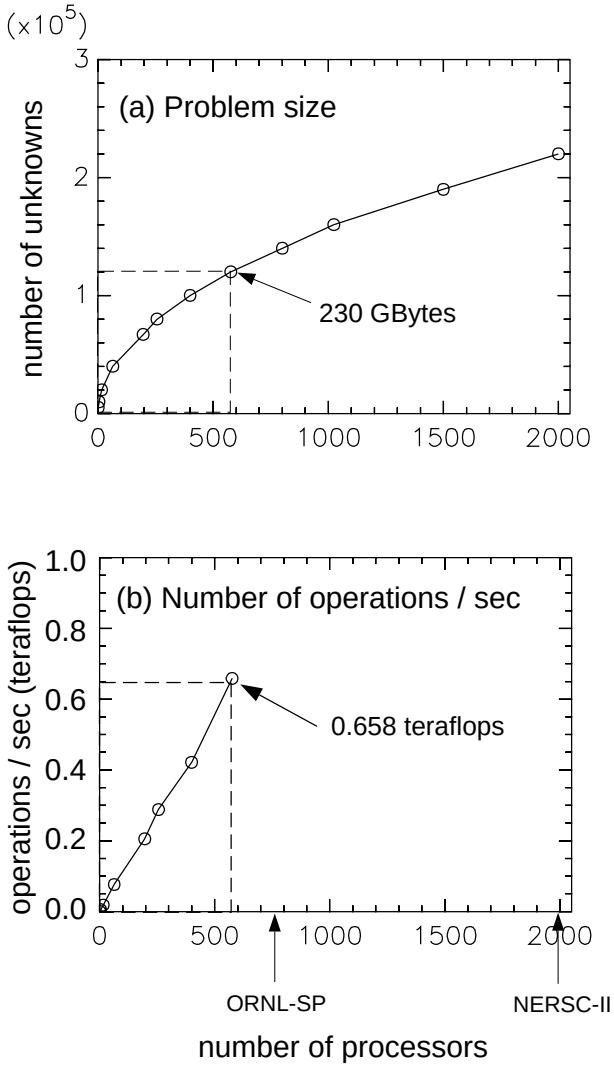

FIG. 1. E. F. Jaeger et al., Phys. Plasmas

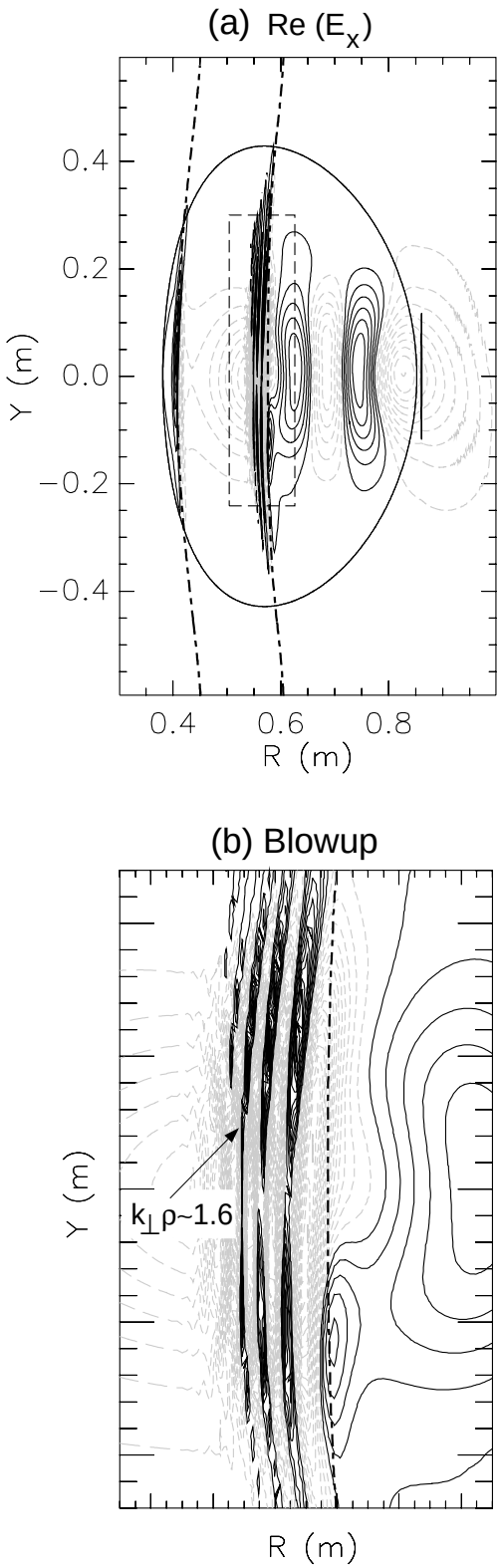

FIG. 2. E. F. Jaeger et al., Phys. Plasmas

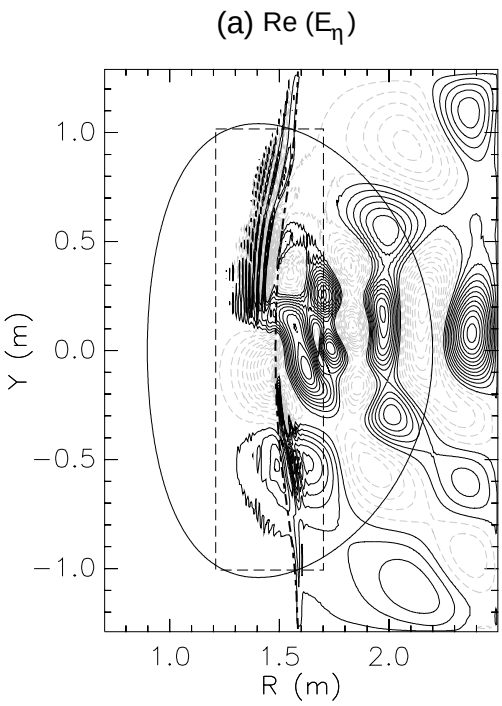

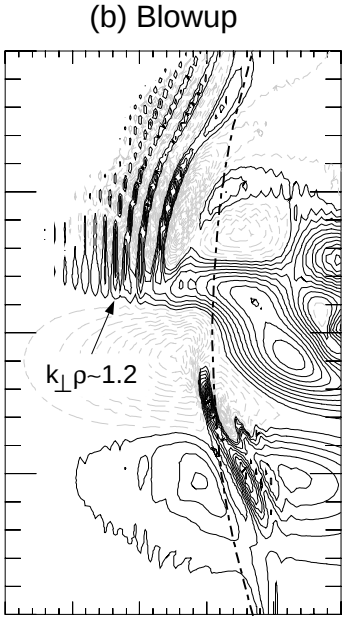

FIG. 3. E. F. Jaeger et al., Phys. Plasmas

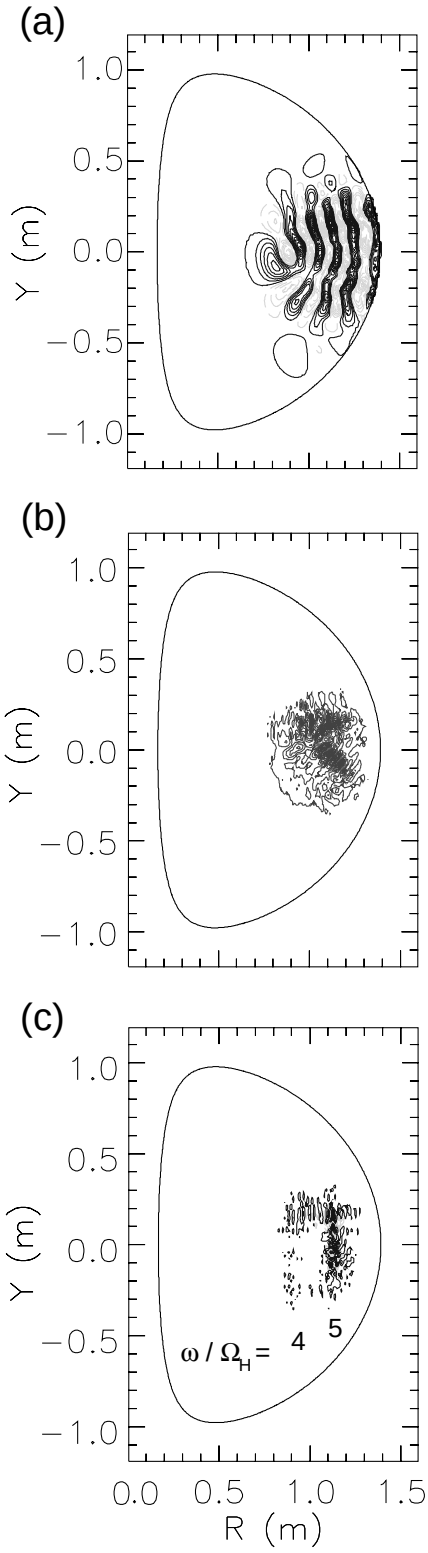

FIG. 4. E. F. Jaeger et al., Phys. Plasmas

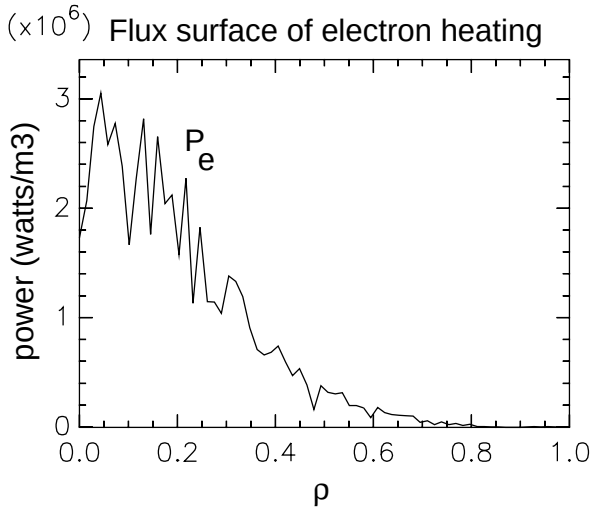

FIG. 5. E. F. Jaeger et al., Phys. Plasmas

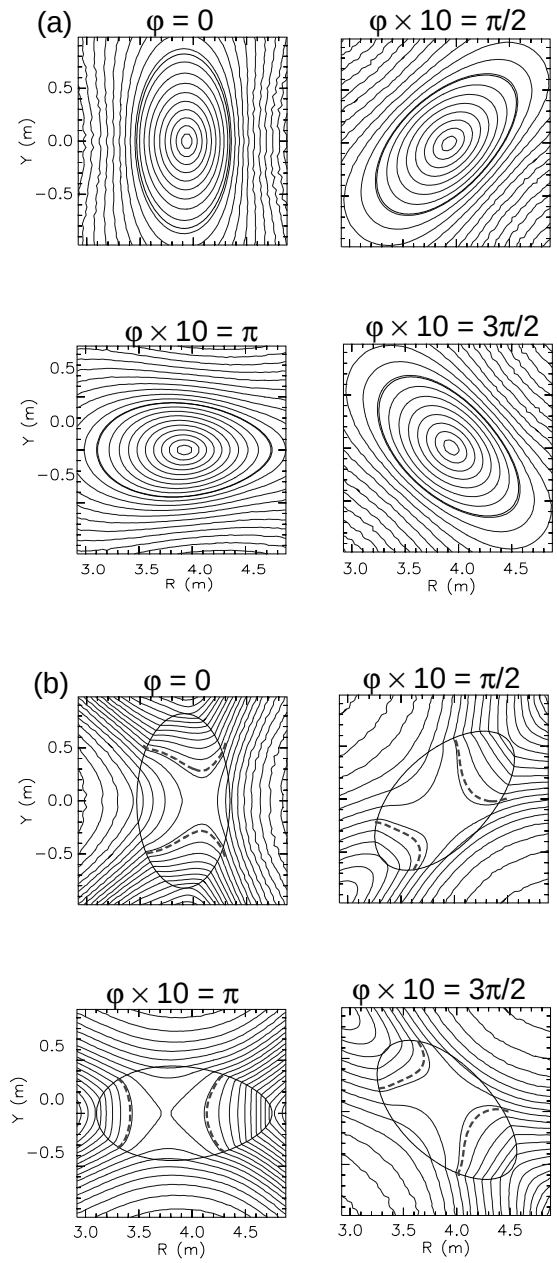

FIG. 6. E. F. Jaeger et al., Phys. Plasmas

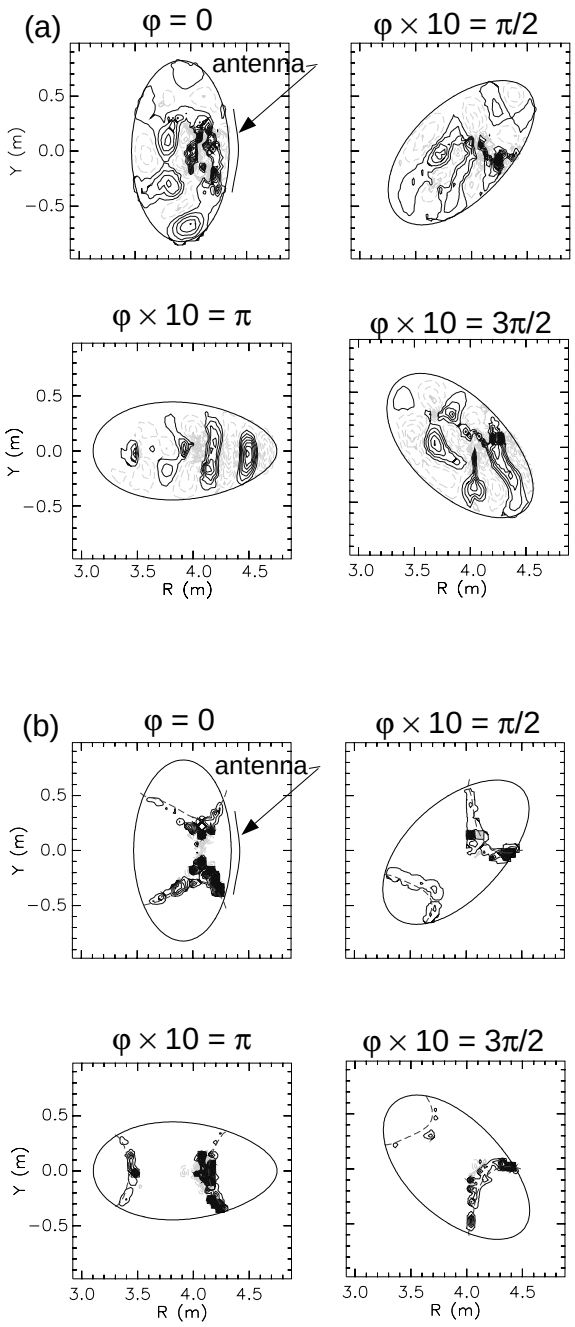

FIG. 7. E. F. Jaeger et al., Phys. Plasmas

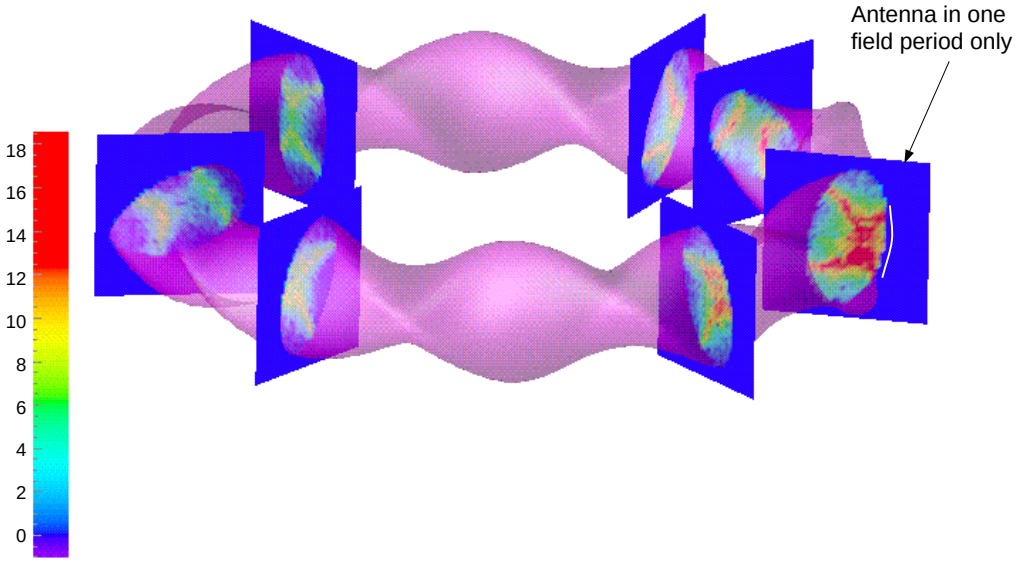

FIG. 8. E. F. Jaeger et al., Phys. Plasmas